

# Sparsity prior for electrical impedance tomography with partial data

Henrik Garde and Kim Knudsen

*Department of Applied Mathematics and Computer Science, Technical University of Denmark,  
2800 Kgs. Lyngby, Denmark*

*(December 2014)*

This paper focuses on prior information for improved sparsity reconstruction in electrical impedance tomography with partial data, i.e. data measured only on subsets of the boundary. Sparsity is enforced using an  $\ell_1$  norm of the basis coefficients as the penalty term in a Tikhonov functional, and prior information is incorporated by applying a spatially distributed regularization parameter. The resulting optimization problem allows great flexibility with respect to the choice of measurement boundaries and incorporation of prior knowledge. The problem is solved using a generalized conditional gradient method applying soft thresholding. Numerical examples show that the addition of prior information in the proposed algorithm gives vastly improved reconstructions even for the partial data problem. The method is in addition compared to a total variation approach.

**Keywords:** Electrical impedance tomography; inverse boundary value problem; ill-posed problem; partial data; sparsity

**AMS Subject Classifications:** 65N20; 65N21

## 1. Introduction

The inverse problem in electrical impedance tomography (EIT) consists of reconstructing an electrical conductivity distribution in the interior of an object from electro-static boundary measurements on the surface of the object. EIT is an emerging technology with applications in medical imaging [1], geophysics [2] and industrial tomography [3]. The underlying mathematical problem is known as the Calderón problem in recognition of Calderón's seminal paper [4].

Consider a bounded domain  $\Omega \subset \mathbb{R}^n$ ,  $n \geq 2$ , with smooth boundary  $\partial\Omega$ . In order to consider partial boundary measurements we introduce the subsets  $\Gamma^N, \Gamma^D \subseteq \partial\Omega$  for the Neumann and Dirichlet data respectively. Let  $\sigma \in L^\infty(\Omega)$  with  $0 < c \leq \sigma$  a.e. denote the conductivity distribution in  $\Omega$ . Applying a boundary current flux  $g$  (Neumann condition) through  $\Gamma^N \subseteq \partial\Omega$  gives rise to the interior electric potential  $u$  characterized as the solution to

$$\nabla \cdot (\sigma \nabla u) = 0 \text{ in } \Omega, \quad \sigma \frac{\partial u}{\partial \nu} = g \text{ on } \partial\Omega, \quad \int_{\Gamma^D} u|_{\partial\Omega} ds = 0, \quad (1.1)$$

where  $\nu$  is an outward unit normal to  $\partial\Omega$ . The latter condition in (1.1) is a grounding of the total electric potential along the subset  $\Gamma^D \subseteq \partial\Omega$ . To be precise we define the spaces

$$L_\diamond^2(\partial\Omega) \equiv \{g \in L^2(\partial\Omega) \mid \int_{\partial\Omega} g ds = 0\},$$

$$H_\diamond^{-1/2}(\partial\Omega) \equiv \{g \in H^{-1/2}(\partial\Omega) \mid \langle g, 1 \rangle = 0\},$$

consisting of boundary functions with mean zero, and the spaces

$$H_{\Gamma^D}^1(\Omega) \equiv \{u \in H^1(\Omega) \mid u|_{\partial\Omega} \in H_{\Gamma^D}^{1/2}(\partial\Omega)\},$$

$$H_{\Gamma^D}^{1/2}(\partial\Omega) \equiv \{f \in H^{1/2}(\partial\Omega) \mid \int_{\Gamma^D} f \, ds = 0\},$$

consisting of functions with mean zero on  $\Gamma^D$  designed to encompass the partial boundary data. Using standard elliptic theory it follows that (1.1) has a unique solution  $u \in H_{\Gamma^D}^1(\Omega)$  for any  $g \in H_{\diamond}^{-1/2}(\partial\Omega)$ . This defines the Neumann-to-Dirichlet map (ND-map)  $\Lambda_{\sigma}$  as an operator from  $H_{\diamond}^{-1/2}(\partial\Omega)$  into  $H_{\Gamma^D}^{1/2}(\partial\Omega)$  by  $g \mapsto u|_{\partial\Omega}$ , and the partial ND-map as  $g \mapsto (\Lambda_{\sigma}g)|_{\Gamma^D}$ .

The data for the classical Calderón problem is the full operator  $\Lambda_{\sigma}$  with  $\Gamma^D = \Gamma^N = \partial\Omega$ . The problem is well-studied and there are numerous publications addressing different aspects of its solution; we mention only a few: the uniqueness and reconstruction problem was solved in [5–10] using the so called complex geometrical optics (CGO) solutions; for a recent survey see [11]. Stability estimates of log type were obtained in [12, 13] and shown to be optimal in [14]. Thus any computational algorithm must rely on regularization. Such computational regularization algorithms following the CGO approach were designed, implemented and analysed in [15–19].

Recently the partial data Calderón problem has been studied intensively. In 3D uniqueness has been proved under certain conditions on  $\Gamma^D$  and  $\Gamma^N$  [20–24], and in 2D the general problem with localized data i.e.  $\Gamma^D = \Gamma^N = \Gamma$  for some, possibly small, subset  $\Gamma \subseteq \partial\Omega$  has been shown to possess uniqueness [25]. Also stability estimates of log-log type have been obtained for the partial problem [26]; this suggests that the partial data problem is even more ill-posed and hence requires more regularization than the full data problem. Recently a computational algorithm for the partial data problem in 2D was suggested and investigated in [27].

A general approach to linear inverse problems with sparsity regularization was given in [28], and in [29, 30] the method was adapted to non-linear problems using a so-called generalized conditional gradient method. In [31–33] the method was applied to the reconstruction problem in EIT with full boundary data. For other approaches to EIT using optimization methods we refer to [34].

In this paper we will focus on the partial data problem for which we develop a reconstruction algorithm based on a least squares formulation with sparsity regularization. The results are twofold: first we extend the full data algorithm of [33] to the case of partial data, second we show how prior information about the spatial location of the perturbation in the conductivity can be used in the design of a spatially varying regularization parameter. We will restrict the treatment to 2D, however everything extends to 3D with some minor assumptions on the regularity of the Neumann data [35].

The data considered here consist of a finite number of Cauchy data taken on the subsets  $\Gamma^D$  and  $\Gamma^N$ , i.e.

$$\{(f_k, g_k) \mid g_k \in H_{\diamond}^{-1/2}(\partial\Omega), \text{supp}(g_k) \subseteq \Gamma^N, f_k = \Lambda_{\sigma}g_k|_{\Gamma^D}\}_{k=1}^K, \quad K \in \mathbb{N}. \quad (1.2)$$

We assume that the true conductivity is given as  $\sigma = \sigma_0 + \delta\sigma$ , where  $\sigma_0$  is a known background conductivity. Define the closed and convex subset

$$\mathcal{A}_0 \equiv \{\delta\gamma \in H_0^1(\Omega) \mid c \leq \sigma_0 + \delta\gamma \leq c^{-1} \text{ a.e. in } \Omega\} \quad (1.3)$$

for some  $c \in (0, 1)$ , and  $\sigma_0 \in H^1(\Omega)$  where  $c \leq \sigma_0 \leq c^{-1}$ . Similarly define

$$\mathcal{A} \equiv \mathcal{A}_0 + \sigma_0 = \{\gamma \in H^1(\Omega) \mid c \leq \gamma \leq c^{-1} \text{ a.e. in } \Omega, \gamma|_{\partial\Omega} = \sigma_0|_{\partial\Omega}\}.$$

The inverse problem is then to approximate  $\delta\sigma \in \mathcal{A}_0$  given the data (1.2).

Let  $\{\psi_j\}$  denote a chosen orthonormal basis for  $H_0^1(\Omega)$ . For sparsity regularization we approximate  $\delta\sigma$  by  $\operatorname{argmin}_{\delta\gamma \in \mathcal{A}_0} \Psi(\delta\gamma)$  using the following Tikhonov functional [33]

$$\Psi(\delta\gamma) \equiv \sum_{k=1}^K R_k(\delta\gamma) + P(\delta\gamma), \quad \delta\gamma \in \mathcal{A}_0, \quad (1.4)$$

with

$$R_k(\delta\gamma) \equiv \frac{1}{2} \|\Lambda_{\sigma_0 + \delta\gamma} g_k - f_k\|_{L^2(\Gamma^D)}^2, \quad P(\delta\gamma) \equiv \sum_{j=1}^{\infty} \alpha_j |c_j|,$$

for  $c_j \equiv \langle \delta\gamma, \psi_j \rangle$ . The regularization parameter  $\alpha_j > 0$  for the sparsity-promoting  $\ell_1$  penalty term  $P$  is distributed such that each basis coefficient can be regularized differently; we will return to this in section 3. It should be noted how easy and natural the use of partial data is introduced in this way, simply by only minimizing the discrepancy on  $\Gamma^D$  on which the Dirichlet data is known and ignoring the rest of the boundary.

This paper is organised as follows: in section 2 we derive the Fréchet derivative of  $R_k$  and reformulate the optimization problem using the generalized conditional gradient method as a sequence of linearized optimization problems. In section 3 we explain the idea of the spatially dependent regularization parameter designed for the use of prior information. Then in section 4 we show the feasibility of the algorithm by several numerical examples, and finally we conclude in section 5.

## 2. Sparse Reconstruction

In this section the sparse reconstruction of  $\delta\sigma$  based on the optimization problem (1.4), is investigated for a bounded domain  $\Omega \subset \mathbb{R}^2$  with smooth boundary  $\partial\Omega$ . The penalty term emphasizes that  $\delta\sigma$  should only be expanded by few basis functions in a given orthonormal basis. Using a distributed regularization parameter, it is possible to further apply prior information about which basis functions that should be included in the expansion of  $\delta\sigma$ . The partial data problem comes into play in the discrepancy term, in which we only fit the data on part of the boundary. Ultimately, this leads to the algorithm given in Algorithm 1 at the end of this section.

Denote by  $F_g(\sigma)$  the unique solution to (1.1) and let  $\mathcal{F}_g(\sigma)$  be its trace (note that  $\Lambda_\sigma g = \mathcal{F}_g(\sigma)$ ). Let  $\gamma \in \mathcal{A}$ ,  $g \in L^p(\partial\Omega) \cap H_\diamond^{-1/2}(\partial\Omega)$  for  $p > 1$ , then following the proofs of Theorem 2.2 and Corollary 2.1 in [32] whilst applying the partial boundary  $\Gamma^D$  we have

$$\lim_{\substack{\|\eta\|_{H^1(\Omega)} \rightarrow 0 \\ \gamma + \eta \in \mathcal{A}}} \frac{\|\mathcal{F}_g(\gamma + \eta) - \mathcal{F}_g(\gamma) - (\mathcal{F}_g)'_{\gamma} \eta\|_{H_{\Gamma^D}^{1/2}(\partial\Omega)}}{\|\eta\|_{H^1(\Omega)}} = 0. \quad (2.1)$$

Here  $(\mathcal{F}_g)'_\gamma$  is the linear map, that maps  $\eta$  to  $w|_{\partial\Omega}$ , where  $w$  is the unique solution to

$$-\nabla \cdot (\gamma \nabla w) = \nabla \cdot (\eta \nabla F_g(\gamma)) \text{ in } \Omega, \quad \sigma \frac{\partial w}{\partial \nu} = 0 \text{ on } \partial\Omega, \quad \int_{\Gamma^D} w|_{\partial\Omega} ds = 0. \quad (2.2)$$

It is noted that  $(\mathcal{F}_g)'_\gamma$  resembles a Fréchet derivative of  $\mathcal{F}_g$  evaluated at  $\gamma$  due to (2.1), however  $\mathcal{A}$  is not a linear vector space, thus the requirement  $\gamma, \gamma + \eta \in \mathcal{A}$ .

The first step in minimizing  $\Psi$  using a gradient descent type iterative algorithm is to determine a derivative to the discrepancy terms  $R_k$ .

LEMMA 2.1 *Let  $\gamma = \sigma_0 + \delta\gamma$  for  $\delta\gamma \in \mathcal{A}_0$ , and  $\chi_{\Gamma^D}$  be a characteristic function on  $\Gamma^D$ . Then*

$$G_k \equiv -\nabla F_{g_k}(\gamma) \cdot \nabla F_{\chi_{\Gamma^D}(\Lambda_\gamma g_k - f_k)}(\gamma) \in L^r(\Omega) \subset H^{-1}(\Omega) \quad (2.3)$$

for some  $r > 1$ , and the Fréchet derivative  $(R_k)'_{\delta\gamma}$  of  $R_k$  on  $H_0^1(\Omega)$  evaluated at  $\delta\gamma$  is given by

$$(R_k)'_{\delta\gamma} \eta = \int_{\Omega} G_k \eta dx, \quad \delta\gamma + \eta \in \mathcal{A}_0. \quad (2.4)$$

*Proof.* For the proof the index  $k$  is suppressed. First it is proved that  $G \in L^r(\Omega)$  for some  $r > 1$ , which is shown by estimates on  $F_g(\gamma)$  and  $F_h(\gamma)$  where  $h \equiv \chi_{\Gamma^D}(\Lambda_\gamma g - f)$ . Note that  $\Lambda_\gamma g \in H_{\Gamma^D}^{1/2}(\partial\Omega)$  and  $f \in L_\diamond^2(\Gamma^D)$ , i.e.  $h \in L_\diamond^2(\partial\Omega) \subset L^2(\partial\Omega) \cap H_\diamond^{-1/2}(\partial\Omega)$ . Now using [32, Theorem 3.1], there exists  $Q > 2$  such that

$$\|F_h(\gamma)\|_{W^{1,q}(\Omega)} \leq C \|h\|_{L^2(\partial\Omega)}, \quad (2.5)$$

where  $q \in (2, Q) \cap [2, 4]$ . Since  $F_g(\gamma) \in H_{\Gamma^D}^1(\Omega)$  then  $|\nabla F_g(\gamma)| \in L^2(\Omega)$ . It has already been established in (2.5) that  $F_h(\gamma) \in W^{1,q}(\Omega)$  for  $q \in (2, \min\{Q, 4\})$ , so  $|\nabla F_h(\gamma)| \in L^q(\Omega)$ . By Hölder's generalized inequality

$$G = -\nabla F_g(\gamma) \cdot \nabla F_h(\gamma) \in L^r(\Omega), \quad \frac{1}{r} = \frac{1}{2} + \frac{1}{q},$$

and as  $q > 2$  then  $r > 1$ . Let  $r'$  be the conjugate exponent to  $r$ , then  $r' \in [1, \infty)$ , i.e. the Sobolev imbedding theorem [36] implies that  $H^1(\Omega) \hookrightarrow L^{r'}(\Omega)$  as  $\Omega \subset \mathbb{R}^2$ . Thus  $G \in (L^{r'}(\Omega))' \subset (H^1(\Omega))' \subset (H_0^1(\Omega))' = H^{-1}(\Omega)$ .

Now it will be shown that  $R'_{\delta\gamma}$  can be identified with  $G$ .  $R'_{\delta\gamma} \eta$  is by the chain rule (utilizing that  $\Lambda_\gamma g = \mathcal{F}_g(\gamma)$ ) given as

$$R'_{\delta\gamma} \eta = \int_{\partial\Omega} \chi_{\Gamma^D}(\Lambda_\gamma g - f) (\mathcal{F}_g)'_\gamma \eta ds, \quad (2.6)$$

where  $\chi_{\Gamma^D}$  is enforcing that the integral is over  $\Gamma^D$ . The weak formulations of (1.1), with Neumann data  $\chi_{\Gamma^D}(\Lambda_\gamma g - f)$ , and (2.2) are

$$\int_{\Omega} \gamma \nabla F_{\chi_{\Gamma^D}(\Lambda_\gamma g - f)}(\gamma) \cdot \nabla v dx = \int_{\partial\Omega} \chi_{\Gamma^D}(\Lambda_\gamma g - f) v|_{\partial\Omega} ds, \quad \forall v \in H^1(\Omega), \quad (2.7)$$

$$\int_{\Omega} \gamma \nabla w \cdot \nabla v dx = - \int_{\Omega} \eta \nabla F_g(\gamma) \cdot \nabla v dx, \quad \forall v \in H^1(\Omega). \quad (2.8)$$

Now by letting  $v \equiv w$  in (2.7) and  $v \equiv F_{\chi_{\Gamma^D}(\Lambda_\gamma g - f)}(\gamma)$  in (2.8), we obtain using the definition  $w|_{\partial\Omega} = (\mathcal{F}_g)'_\gamma \eta$  that

$$\begin{aligned} R'_{\delta\gamma} \eta &= \int_{\partial\Omega} \chi_{\Gamma^D}(\Lambda_\gamma g - f) (\mathcal{F}_g)'_\gamma \eta \, ds = \int_{\Omega} \gamma \nabla F_{\chi_{\Gamma^D}(\Lambda_\gamma g - f)}(\gamma) \cdot \nabla w \, dx \\ &= - \int_{\Omega} \eta \nabla F_g(\gamma) \cdot \nabla F_{\chi_{\Gamma^D}(\Lambda_\gamma g - f)}(\gamma) \, dx = \int_{\Omega} G \eta \, dx. \end{aligned}$$

□

*Remark 2.2* It should be noted that  $(R_k)'_{\delta\gamma}$  is related to the Fréchet derivative  $\Lambda'_\gamma$  of  $\gamma \mapsto \Lambda_\gamma$  evaluated at  $\gamma$ , by  $(R_k)'_{\delta\gamma} \eta = \int_{\Gamma^D} (\Lambda_\gamma g_k - f_k) \Lambda'_\gamma[\eta] g_k \, ds$ .

Define

$$R'_{\delta\gamma} \equiv \sum_{k=1}^K (R_k)'_{\delta\gamma} = - \sum_{k=1}^K \nabla F_{g_k}(\gamma) \cdot \nabla F_{\chi_{\Gamma^D}(\Lambda_\gamma g_k - f_k)}(\gamma).$$

For a gradient type descent method, we seek to find a direction  $\eta$  for which the discrepancy decreases. As  $R'_{\delta\gamma} \in H^{-1}(\Omega)$  it is known from Riesz' representation theorem that there exists a unique function in  $H_0^1(\Omega)$ , denoted by  $\nabla_s R(\delta\gamma)$ , such that

$$R'_{\delta\gamma} \eta = \langle \nabla_s R(\delta\gamma), \eta \rangle_{H^1(\Omega)}, \quad \eta \in H_0^1(\Omega). \quad (2.9)$$

Now  $\eta \equiv -\nabla_s R(\delta\gamma)$  points in the steepest descend direction among the viable directions. Furthermore, since  $\nabla_s R(\delta\gamma)|_{\partial\Omega} = 0$  the boundary condition  $\delta\sigma|_{\partial\Omega} = 0$  will automatically be fulfilled for the approximation. In [37]  $\nabla_s R(\delta\gamma)$  is called a Sobolev-gradient, and it is the unique solution to

$$(-\Delta + 1)v = R'_{\delta\gamma} \text{ in } \Omega, \quad v = 0 \text{ on } \partial\Omega,$$

for which (2.9) is the weak formulation. In each iteration step we need to determine a step size  $s_i$  for an algorithm resembling a steepest descent  $\delta\gamma_{i+1} = \delta\gamma_i - s_i \nabla_s R(\delta\gamma_i)$ . Here a Barzilai-Borwein step size rule [33, 38, 39] will be applied, for which we determine  $s_i$  such that  $\frac{1}{s_i}(\delta\gamma_i - \delta\gamma_{i-1}) = \frac{1}{s_i}(\gamma_i - \gamma_{i-1}) \simeq \nabla_s R(\delta\gamma_i) - \nabla_s R(\delta\gamma_{i-1})$  in the least-squares sense

$$s_i \equiv \underset{s}{\operatorname{argmin}} \|s^{-1}(\delta\gamma_i - \delta\gamma_{i-1}) - (\nabla_s R(\delta\gamma_i) - \nabla_s R(\delta\gamma_{i-1}))\|_{H^1(\Omega)}^2. \quad (2.10)$$

Assuming that  $\langle \delta\gamma_i - \delta\gamma_{i-1}, \nabla_s R(\delta\gamma_i) - \nabla_s R(\delta\gamma_{i-1}) \rangle_{H^1(\Omega)} \neq 0$  yields

$$s_i = \frac{\|\delta\gamma_i - \delta\gamma_{i-1}\|_{H^1(\Omega)}^2}{\langle \delta\gamma_i - \delta\gamma_{i-1}, \nabla_s R(\delta\gamma_i) - \nabla_s R(\delta\gamma_{i-1}) \rangle_{H^1(\Omega)}}. \quad (2.11)$$

A maximum step size  $s_{\max}$  is enforced to avoid the situations where  $\langle \delta\gamma_i - \delta\gamma_{i-1}, \nabla_s R(\delta\gamma_i) - \nabla_s R(\delta\gamma_{i-1}) \rangle_{H^1(\Omega)} \simeq 0$ .

With inspiration from [39],  $s_i$  will be initialized by (2.11), after which it is thresholded to lie in  $[s_{\min}, s_{\max}]$ , for positive constants  $s_{\min}$  and  $s_{\max}$ . It is noted in [39] that Barzilai-Borwein type step rules lead to faster convergence if we do not restrict  $\Psi$  to decrease in every iteration. Allowing an occasional increase in  $\Psi$  can be used to avoid places where

the method has to take many small steps to ensure the decrease of  $\Psi$ . Therefore, one makes sure that the following so called weak monotonicity is satisfied, which compares  $\Psi(\delta\gamma_{i+1})$  with the most recent  $M$  steps. Let  $\tau \in (0, 1)$  and  $M \in \mathbb{N}$ , then  $s_i$  is said to satisfy the weak monotonicity with respect to  $M$  and  $\tau$  if the following is satisfied [39]

$$\Psi(\delta\gamma_{i+1}) \leq \max_{i-M+1 \leq j \leq i} \Psi(\delta\gamma_j) - \frac{\tau}{2s_i} \|\delta\gamma_{i+1} - \delta\gamma_i\|_{H^1(\Omega)}^2. \quad (2.12)$$

If (2.12) is not satisfied, the step size  $s_i$  is reduced until this is the case. To solve the non-linear minimization problem for (1.4) we iteratively solve the following linearized problem

$$\zeta_{i+1} \equiv \operatorname{argmin}_{\delta\gamma \in H_0^1(\Omega)} \left[ \frac{1}{2} \|\delta\gamma - (\delta\gamma_i - s_i \nabla_s R(\delta\gamma_i))\|_{H^1(\Omega)}^2 + s_i \sum_{j=1}^{\infty} \alpha_j |c_j| \right], \quad (2.13)$$

$$\delta\gamma_{i+1} \equiv \mathcal{P}_{\mathcal{A}_0}(\zeta_{i+1}).$$

Here  $\{\psi_j\}$  is an orthonormal basis for  $H_0^1(\Omega)$  in the  $H^1$ -metric, and  $\mathcal{P}_{\mathcal{A}_0}$  is a projection of  $H_0^1(\Omega)$  onto  $\mathcal{A}_0$  to ensure that (1.1) is solvable (note that  $H_0^1(\Omega)$  does not imbed into  $L^\infty(\Omega)$ , i.e.  $\zeta_{i+1}$  may be unbounded). By use of the map  $\mathcal{S}_\beta : \mathbb{R} \rightarrow \mathbb{R}$  defined below, known as the soft shrinkage/thresholding map with threshold  $\beta > 0$ ,

$$\mathcal{S}_\beta(x) \equiv \operatorname{sgn}(x) \max\{|x| - \beta, 0\}, \quad x \in \mathbb{R}, \quad (2.14)$$

the solution to (2.13) is easy to find directly (see also [28, Section 1.5]):

$$\zeta_{i+1} = \sum_{j=1}^{\infty} \mathcal{S}_{s_i \alpha_j}(d_j) \psi_j, \quad (2.15)$$

where  $d_j \equiv \langle \delta\gamma_i - s_i \nabla_s R(\delta\gamma_i), \psi_j \rangle_{H^1(\Omega)}$  are the basis coefficients for  $\delta\gamma_i - s_i \nabla_s R(\delta\gamma_i)$ .

The projection  $\mathcal{P}_{\mathcal{A}_0} : H_0^1(\Omega) \rightarrow \mathcal{A}_0$  is defined as

$$\mathcal{P}_{\mathcal{A}_0}(v) \equiv T_c(\sigma_0 + v) - \sigma_0, \quad v \in H_0^1(\Omega),$$

where  $T_c$  is the following truncation that depends on the constant  $c \in (0, 1)$  in (1.3)

$$T_c(v) \equiv \begin{cases} c & \text{where } v < c \text{ a.e.}, \\ c^{-1} & \text{where } v > c^{-1} \text{ a.e.}, \\ v & \text{else.} \end{cases}$$

Since  $\sigma_0 \in H^1(\Omega)$  and  $c \leq \sigma_0 \leq c^{-1}$ , it follows directly from [40, Lemma 1.2] that  $T_c$  and  $\mathcal{P}_{\mathcal{A}_0}$  are well-defined, and it is easy to see that  $\mathcal{P}_{\mathcal{A}_0}$  is a projection. It should also be noted that  $0 \in \mathcal{A}_0$  since  $c \leq \sigma_0 \leq c^{-1}$ , thus we may choose  $\delta\gamma_0 \equiv 0$  as the initial guess in the algorithm.

The algorithm is summarized in Algorithm 1. In this paper the stopping criteria is when the step size  $s_i$  gets below a threshold  $s_{\text{stop}}$ .

*Remark 2.3* Note that  $\sum_j \langle \delta\gamma_i - s_i \nabla_s R(\delta\gamma_i), \psi_j \rangle_{H^1(\Omega)} \psi_j$  corresponds to only having the discrepancy term in (2.13), while the penalty term corresponds to changing these coefficients with the soft thresholding.

*Remark 2.4* The non-linearity of  $\gamma \mapsto \Lambda_\gamma$  leads to a non-convex discrepancy term, i.e.  $\Psi$  is non-convex. So the best we can hope is to find a local minimum.

---

**Algorithm 1** Sparse Reconstruction for Partial Data EIT

---

Set  $\delta\gamma_0 := 0$ .

**while** stopping criteria not reached **do**

  Set  $\gamma_i := \sigma_0 + \delta\gamma_i$ .

  Compute  $\Psi(\delta\gamma_i)$ .

  Compute  $R'_{\delta\gamma_i} := -\sum_{k=1}^K \nabla F_{g_k}(\gamma_i) \cdot \nabla F_{\chi_{\Gamma^D}(\Lambda_{\gamma_i} g_k - f_k)}(\gamma_i)$ .

  Compute  $\nabla_s R(\delta\gamma_i) \in H_0^1(\Omega)$  such that  $R'_{\delta\gamma_i} \eta = \langle \nabla_s R(\delta\gamma_i), \eta \rangle_{H^1(\Omega)}$ .

  Compute step length  $s_i$  by (2.11), and decrease it till (2.12) is satisfied.

  Compute the basis coefficients  $\{d_j\}_{j=1}^\infty$  for  $\delta\gamma_i - s_i \nabla_s R(\delta\gamma_i)$ .

  Update  $\delta\gamma_{i+1} := \mathcal{P}_{\mathcal{A}_0} \left( \sum_{j=1}^\infty \mathcal{S}_{s_i \alpha_j}(d_j) \psi_j \right)$ .

**end while**

Return final iterate of  $\delta\gamma$ .

---

*Remark 2.5* The main computational cost lies in computing  $R'_{\delta\gamma_i}$ , which involves solving  $2K$  well-posed PDE's (note that  $F_{g_k}(\gamma_i)$  can be reused from the evaluation of  $\Psi$ ). It should be noted that each of the  $2K$  problems consists of solving the same problem, but with different boundary conditions, which leads to only having to assemble and factorize the FEM matrix once per iteration.

### 3. Prior Information

Prior information is typically introduced in the penalty term  $P$  for Tikhonov-like functionals, and here the regularization parameter determines how much this prior information is enforced. In the case of sparsity regularization this implies knowledge of how sparse we expect the solution is in general. Instead of applying the same prior information for each basis function, a distributed parameter is applied. Let

$$\alpha_j \equiv \alpha \mu_j,$$

where  $\alpha$  is a usual regularization parameter, corresponding to the case where no prior information is considered about specific basis functions. The  $\mu_j \in (0, 1]$  will be used to weigh the penalty depending on whether a specific basis function should be included in the expansion of  $\delta\sigma$ . The  $\mu_j$  are chosen as

$$\mu_j = \begin{cases} 1, & \text{no prior on } c_j, \\ \sim 0, & \text{prior that } c_j \neq 0, \end{cases}$$

i.e. if we know that a coefficient in the expansion of  $\delta\sigma$  should be non-zero, we can choose to penalize that coefficient less.

#### 3.1. Applying the FEM basis

In order to improve the sparsity solution for finding small inclusions, it seems appropriate to include prior information about the support of the inclusions. There are different

methods available for obtaining such information assuming piecewise constant conductivity [41, 42] or real analytic conductivity [43]. An example of the reconstruction of  $\text{supp } \delta\sigma$  is shown in figure 3.1, where it is observed that numerically it is possible to reconstruct a reasonable convex approximation to the support. Thus, it is possible to acquire estimates of  $\text{supp } \delta\sigma$  *for free*, in the sense that it is gained directly from the data without further assumptions.

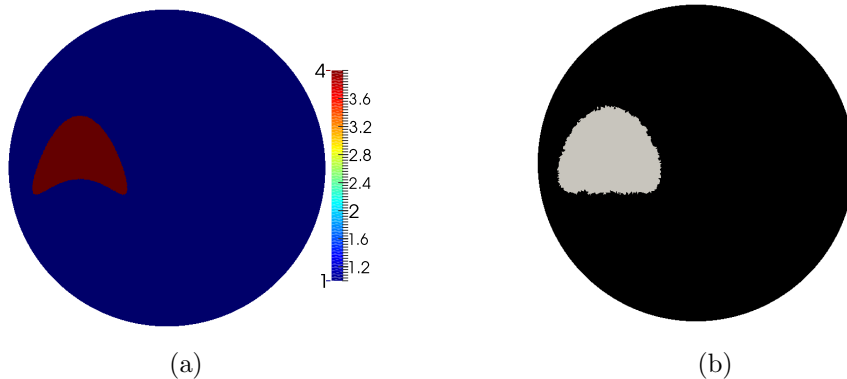


Figure 3.1. **(a)**: Phantom with kite-shaped piecewise constant inclusion  $\delta\sigma$ . **(b)**: Reconstruction of  $\text{supp } \delta\sigma$  using monotonicity relations from the approach in [42] by use of simulated noiseless data.

Another approach is to consider other reconstruction methods such as total variation regularization that tends to give good approximations to the support, but has issues with reconstructing the contrast if the amplitude of  $\delta\sigma$  is large as seen in section 4.3. The idea is to be able to apply such information in the sparsity algorithm in order to get good contrast reconstruction while maintaining the correct support, even for the partial data problem.

Suppose that as a basis we consider a finite element method (FEM) basis  $\{\psi_j\}_{j=1}^N$  for the subspace  $V_h \subseteq H_0^1(\Omega)$  of piecewise affine elements. This basis comprises basis functions that are piecewise affine with degrees of freedom at the mesh nodes, i.e.  $\psi_j(x_k) = \delta_{j,k}$  at mesh node  $x_k$  in the applied mesh. Let  $\delta\sigma \in V_h$ , then  $\delta\sigma(x) = \sum_j \delta\sigma(x_j)\psi_j(x)$ , i.e. for each node there is a basis function for which the coefficient contains local information about the expanded function; this is convenient when applying prior information about the support of an inclusion. Note that the FEM basis functions are not mutually orthogonal, since basis functions corresponding to neighbouring nodes are non-negative and have overlapping support. However, for any non-neighbouring pair of nodes the corresponding basis functions are orthogonal.

When applying the FEM basis for mesh nodes  $\{x_j\}_{j=1}^N$ , the corresponding functional is

$$\Psi(\delta\gamma) = \frac{1}{2} \sum_{k=1}^K \|\Lambda_{\sigma_0 + \delta\gamma} g_k - f_k\|_{L^2(\Gamma^D)}^2 + \sum_{j=1}^N \alpha_j |\delta\gamma(x_j)|.$$

It is evident that the penalty corresponds to determining inclusions with small support, and prior information on the sparsity corresponds to prior information on the support of  $\delta\sigma$ . We cannot directly utilize (2.15) due to the FEM basis not being an orthonormal

basis for  $H_0^1(\Omega)$ , and instead we suggest the following iteration step:

$$\begin{aligned}\zeta_{i+1}(x_j) &= \mathcal{S}_{s_i \alpha_j / \|\psi_j\|_{L^1(\Omega)}}(\delta\gamma_i(x_j) - s_i \nabla_s R(\delta\gamma_i)(x_j)), \quad j = 1, 2, \dots, N, \\ \delta\gamma_{i+1} &= \mathcal{P}_{\mathcal{A}_0}(\zeta_{i+1}).\end{aligned}\tag{3.1}$$

Note that the regularization parameter will depend quite heavily on the discretization of the mesh, i.e. for the same domain a good regularization parameter  $\alpha$  will be much larger on a coarse mesh than on a fine mesh. This is quite inconvenient, and instead we can weigh the regularization parameter according to the mesh cells, by having  $\alpha_j \equiv \alpha \beta_j \mu_j$ . This leads to a discretization of a weighted  $L^1$ -norm penalty term:

$$\alpha \int_{\Omega} f_{\mu} |\delta\sigma| dx \simeq \alpha \sum_j \beta_j \mu_j |\delta\sigma(x_j)|,$$

where  $f_{\mu} : \Omega \rightarrow (0, 1]$  is continuous and  $f_{\mu}(x_j) = \mu_j$ . For a triangulated mesh, the weights  $\beta_j$  consists of the node area computed in 2D as 1/3 of the area of  $\text{supp } \psi_j$ . This corresponds to splitting each cell's area evenly amongst the nodes, and it will not lead to instability on a regular mesh. This will make the choice of  $\alpha$  almost independent of the mesh.

*Remark 3.1* The corresponding algorithm with the FEM basis is the same as Algorithm 1, except that the update is applied via (3.1).

#### 4. Numerical Examples

In this section we illustrate, through several examples, the numerical algorithm implemented using the finite element library FEniCS [44]. First we consider the full data case  $\Gamma^D = \Gamma^N = \partial\Omega$  without and with prior information, and then we do the same for the partial data case. Finally, a brief comparison is made with another sparsity promoting method based on total variation.

For the following examples  $\Omega$  is the unit disk in  $\mathbb{R}^2$ . The regularization parameter  $\alpha$  is chosen manually by trial and error. The other parameters are  $\sigma_0 \equiv 1$ ,  $M = 5$ ,  $\tau = 10^{-5}$ ,  $s_{\min} = 1$ ,  $s_{\max} = 1000$ , and the stopping criteria is when the step size is below  $s_{\text{stop}} = 10^{-3}$ .  $K = 10$  and the applied Neumann data will be of the form  $g_n^c(\theta) \equiv \cos(n\theta)$  and  $g_n^s(\theta) \equiv \sin(n\theta)$  for  $n = 1, \dots, 5$  and  $\theta$  being the angular variable. For the partial data an interval  $\Gamma = \Gamma^N = \Gamma^D = \{\theta \in (\theta_1, \theta_2)\}$  is considered, and  $g_n^c$  and  $g_n^s$  are scaled and translated such that they have  $n$  periods in the interval.

When applying prior information, the coefficients  $\mu_j$  are chosen as  $10^{-2}$  where the support of  $\delta\sigma$  is assumed, and 1 elsewhere. It should be noted that in order to get fast transitions for sharp edges when prior information is applied, a local mesh refinement is used during the iterations to refine the mesh where  $|\nabla\delta\sigma|$  is large.

For the simulated Dirichlet data, the forward problem is computed on a very fine mesh, and afterwards interpolated onto a different much coarser mesh in order to avoid inverse crimes. White Gaussian noise has been added to the Dirichlet data  $\{f_k\}_{k=1}^K$  on the discrete nodes on the boundary of the mesh. The standard deviation of the noise is chosen as  $\epsilon \max_k \max_{x_j \in \Gamma^D} |f_k(x_j)|$  as in [33], where the noise level is fixed as  $\epsilon = 10^{-2}$  (corresponding to 1% noise) unless otherwise stated.

Figure 4.1 shows the numerical phantoms: where one is a simple circular inclusion, another is the non-convex kite-shaped phantom. Finally, we also shortly investigate the case of multiple smoother inclusions.

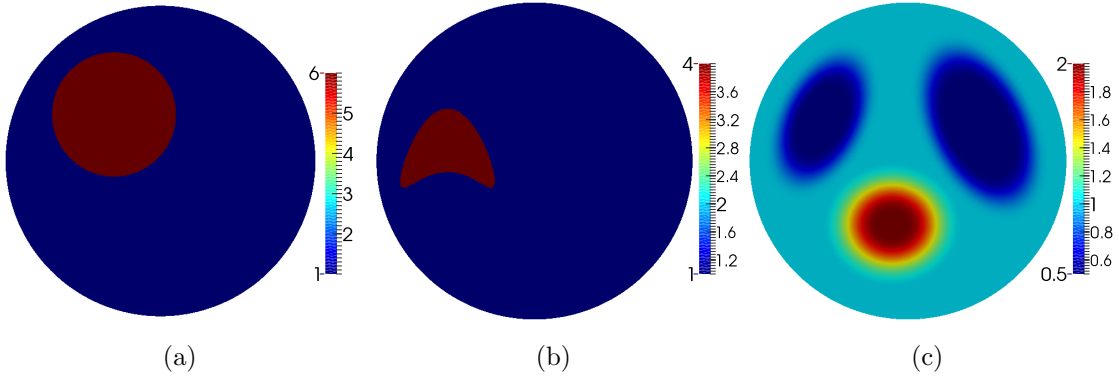


Figure 4.1. **(a)**: Circular piecewise constant inclusion. **(b)**: Kite-shaped piecewise constant inclusion. **(c)**: Multiple  $C^2$  inclusions.

#### 4.1. Full Boundary Data

For  $\Gamma^D = \Gamma^N = \partial\Omega$  it is possible to get quite good reconstructions of both shape and contrast for the convex inclusions as seen in figure 4.2, and for the case with multiple inclusions there is a reasonable separation of the inclusions.

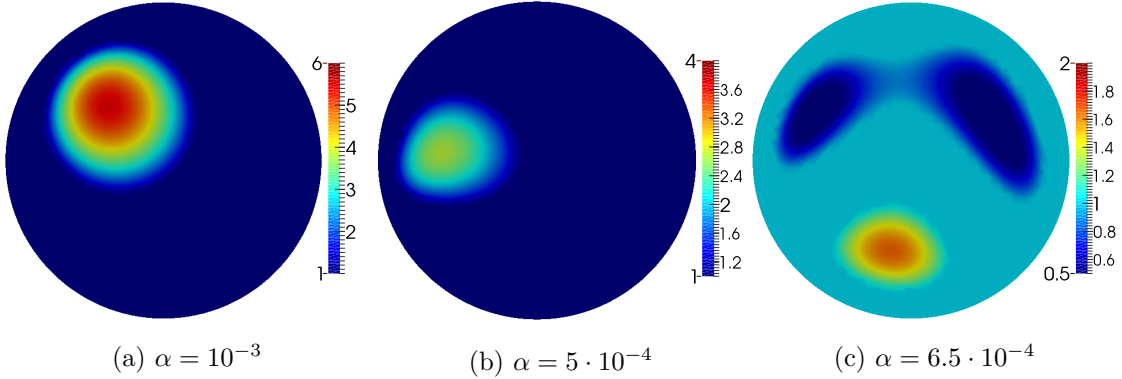


Figure 4.2. Sparse reconstruction of the phantoms in figure 4.1.

For the kite-shaped phantom we only get what seems like a convex approximation of the shape. It is seen in [33] that the algorithm is able to reconstruct some types of non-convex inclusions such as the hole in a ring-shaped phantom, however those inclusions are much larger which makes it easier to distinguish from similar convex inclusions.

We note that the method is very stable towards noise. In figure 4.3 it is shown how unreasonable amounts of noise only leads to small deformations in the shape of the reconstructed inclusion.

In order to investigate the use of prior information we consider the phantom in figure 4.1(a), and let  $B(r)$  denote a ball centered at the correct inclusion and with radius  $r$ . Now we can investigate reconstructions with prior information assuming that the support of  $\delta\sigma$  is  $\overline{B((1 + \delta r)r^*)}$  for  $r^*$  being the correct radius of the inclusion. Figure 4.4 shows that underestimating the support of the inclusion  $\delta r < 0$  is heavily enforced, and the contrast is vastly overestimated in the reconstruction as shown in figure 4.5 (note that this can not be seen in figure 4.4 as the color scale for the phantom is applied).

Interestingly, when overestimating the support, the contrast and support of the reconstructed inclusion does not suffer particularly. Intuitively, this corresponds to increasing  $\delta r$  such that the assumed support of  $\delta\sigma$  contains the entire domain  $\Omega$ , which corresponds to the case with no prior information. For a subset  $E \subseteq \Omega$  denote by  $\sigma_E \equiv |E|^{-1} \int_E \sigma dx$

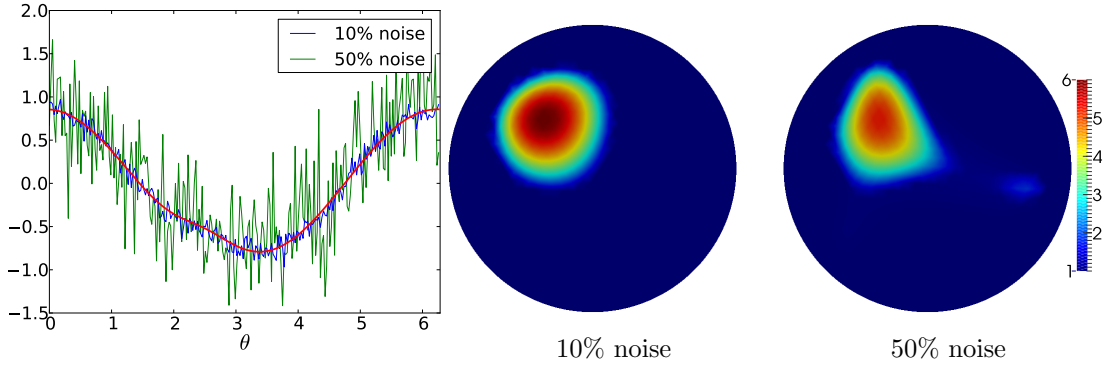


Figure 4.3. **Left:** Dirichlet data corresponding to  $g = \cos(\theta)$  for the phantom in figure 4.1(a), with 10% and 50% noise level. **Middle:** reconstruction for 10% noise level. **Right:** reconstruction for 50% noise level.

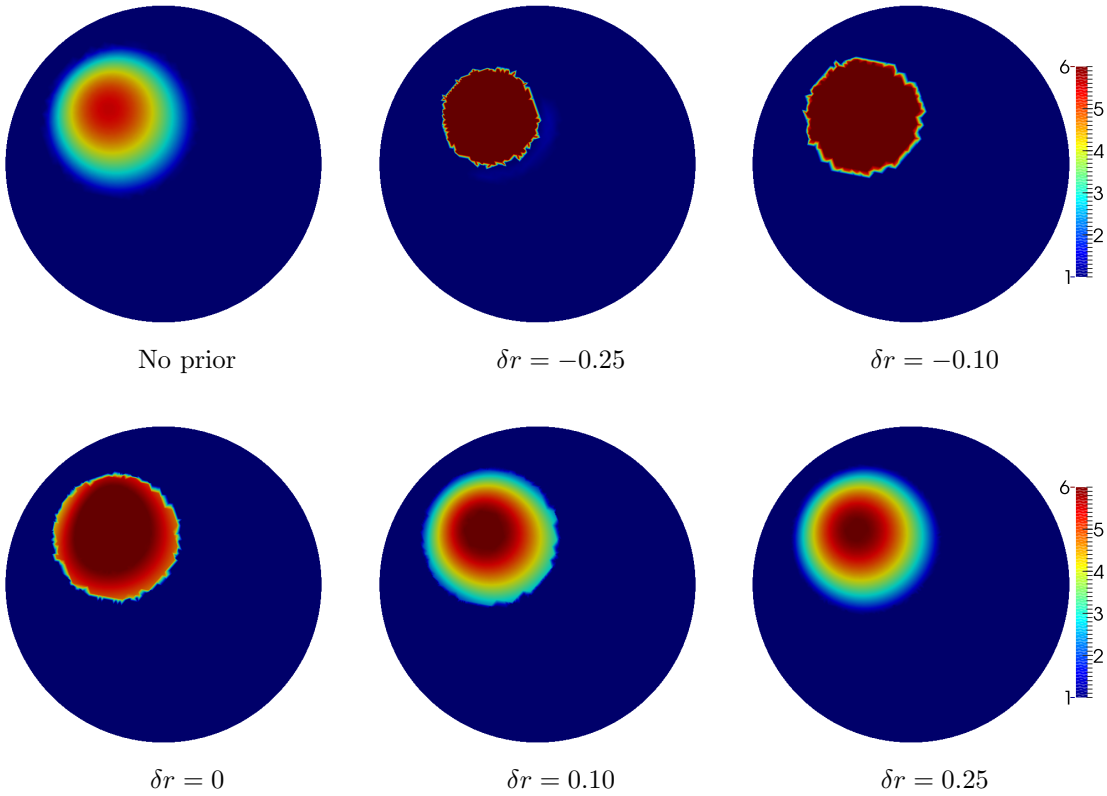


Figure 4.4. Sparse reconstruction of the phantom in figure 4.1(a) for varying  $\delta r$ . The colorbar is truncated at  $[1, 6]$ .

the average of  $\sigma$  on  $E$ , and denote by  $\sigma_{\max} \equiv \max_j |\sigma(x_j)|$  the maximum of  $\sigma$  on the mesh nodes. Then figure 4.5 gives a good indication of the aforementioned intuition, where around  $\delta r = 0$  both  $\sigma_B$  and  $\sigma_{\max}$  levels off around the correct contrast of the inclusion (the red line) and stays there for  $\delta r > 0$ . It should be noted that even a 25% overestimation of the support leads to a better contrast in the reconstruction than if no prior information was applied, as seen in figure 4.4.

Having an overestimation of the support for  $\delta\sigma$  also seems to be a reasonable assumption. Definitely there is the case of no prior information which means that  $\text{supp } \delta\sigma$  is assumed to be  $\Omega$ . If the estimation comes from another method such as total variation

regularization, then the support is typically slightly overestimated while the contrast suffers [45]. Thus we can use the overestimated support to get a good localisation and contrast reconstruction simultaneously.

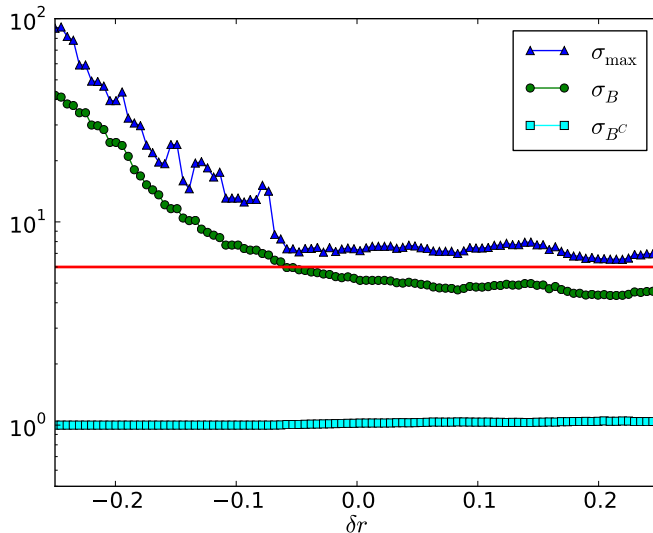


Figure 4.5. Behaviour of sparsity reconstruction based on the phantom in figure 4.1(a) for varying  $\delta r$ .

Figure 4.6 shows how the reconstruction of the kite-shaped phantom can be vastly improved. Note that not only is  $\text{supp } \delta\sigma$  better approximated, but the contrast is also highly improved. It is not surprising that we can achieve an almost perfect reconstruction if  $\text{supp } \delta\sigma$  is exactly known, however it is a good benchmark to compare the cases for the overestimated support as it shows how well the method can possibly do.

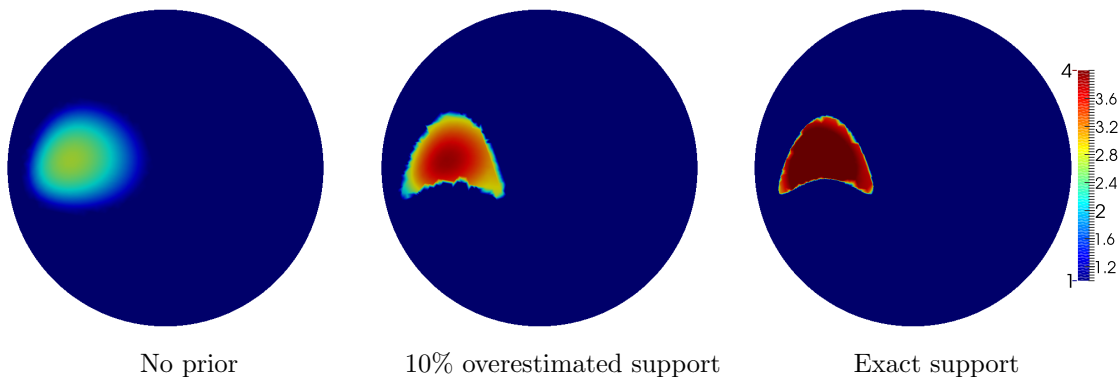


Figure 4.6. Sparse reconstruction of the phantom in figure 4.1(b).

## 4.2. Partial Boundary Data

For the partial data problem we choose  $\Gamma = \Gamma^D = \Gamma^N = \{\theta \in (\theta_1, \theta_2)\}$  for  $0 \leq \theta_1 < \theta_2 \leq 2\pi$ .

In figure 4.7 we observe that with data on the top half of the unit circle it is actually possible to get very good contrast and also reasonable localization of the two large inclusions. There is still a clear separation of the inclusions, while the small inclusion is not reconstructed at all. With data on the bottom half the small inclusion is reconstructed

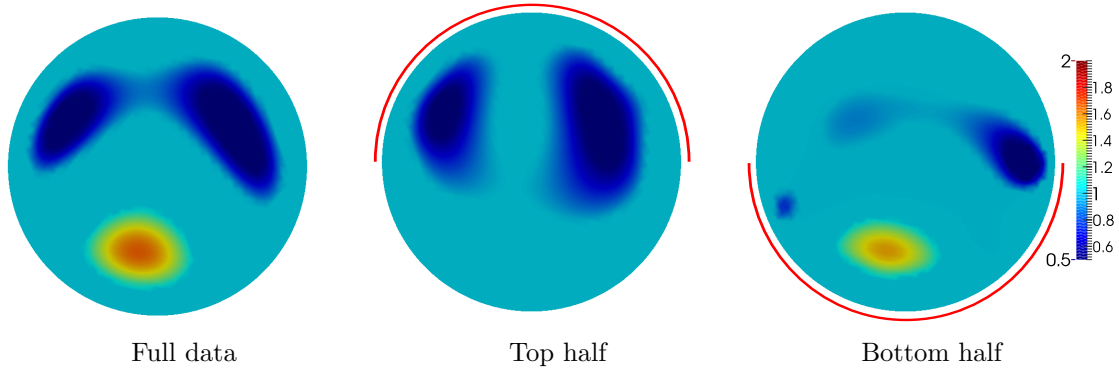


Figure 4.7. Sparse reconstruction of the phantom in figure 4.1(c). **Left:**  $\Gamma = \partial\Omega$ . **Middle:**  $(\theta_1, \theta_2) = (0, \pi)$ . **Right:**  $(\theta_1, \theta_2) = (\pi, 2\pi)$ .

almost as well as with full boundary data, but the larger inclusions are only vaguely visible. This is the kind of behaviour that is expected from partial data EIT, and in practice it implies that we can only expect reasonable reconstruction close to where the measurements are taken.

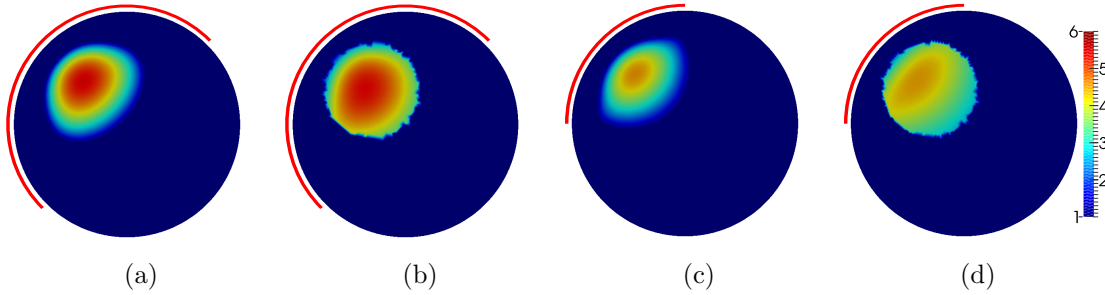


Figure 4.8. Sparse reconstruction of the phantom in figure 4.1(a). **(a):** 50% boundary data, no prior. **(b):** 50% boundary data with 5% overestimated support. **(c):** 25% boundary data, no prior. **(d):** 25% boundary data with 5% overestimated support.

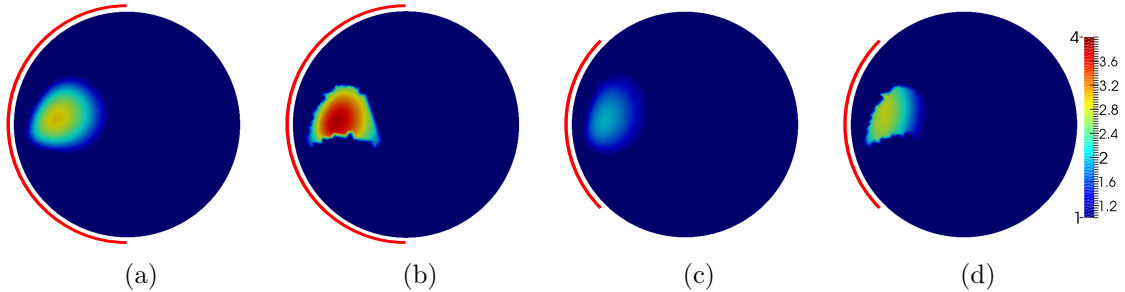


Figure 4.9. Sparse reconstruction of the phantom in figure 4.1(b). **(a):** 50% boundary data, no prior. **(b):** 50% boundary data with 10% overestimated support. **(c):** 25% boundary data, no prior. **(d):** 25% boundary data with 10% overestimated support.

In figure 4.8 and figure 4.9 panels (a) and (c) it is observed that as the length of  $\Gamma$  becomes smaller, the reconstructed shape of the inclusion is rapidly deformed. By including prior information about the support of  $\delta\sigma$ , it is possible to rectify the deformation of the shape, and get reconstructions with almost the correct shape but with a slightly worse reconstructed contrast compared to full boundary data reconstructions. This is observed for the ball and kite-shaped inclusions in figure 4.8 and figure 4.9.

### 4.3. Comparison with Total Variation Regularization

Another sparsity promoting method is total variation (TV) regularization, which promotes a sparse gradient in the solution. This can be achieved by minimizing the functional

$$\Psi_{\text{TV}}(\delta\gamma) \equiv \sum_{k=1}^K R_k(\delta\gamma) + P_{\text{TV}}(\delta\gamma), \quad \delta\gamma \in \mathcal{A}_0, \quad (4.1)$$

where the discrepancy terms  $R_k$  remains the same as in (1.4), but the penalty term is now given by

$$P_{\text{TV}}(\delta\gamma) \equiv \alpha \int_{\Omega} \sqrt{|\nabla\delta\gamma|^2 + b} dx. \quad (4.2)$$

Here  $b > 0$  is a constant that implies that  $P_{\text{TV}}$  is differentiable, but chosen small such that  $P_{\text{TV}}$  approximates  $\alpha \int_{\Omega} |\nabla\delta\gamma| dx$ .

For the numerical examples, the piecewise constant phantoms in figure 4.1(a) and figure 4.1(b) are used, with the same noise level as in the previous sections. The value  $b = 10^{-5}$  is used for the penalty term in all the examples.

It should be noted that the color scale in the following examples is not the same scale as for the phantoms, unlike the previous reconstructions. This is because the TV reconstructions have a significantly lower contrast, in particular for the partial data reconstructions, and would be visually difficult to distinguish from the background conductivity in the correct color scale.

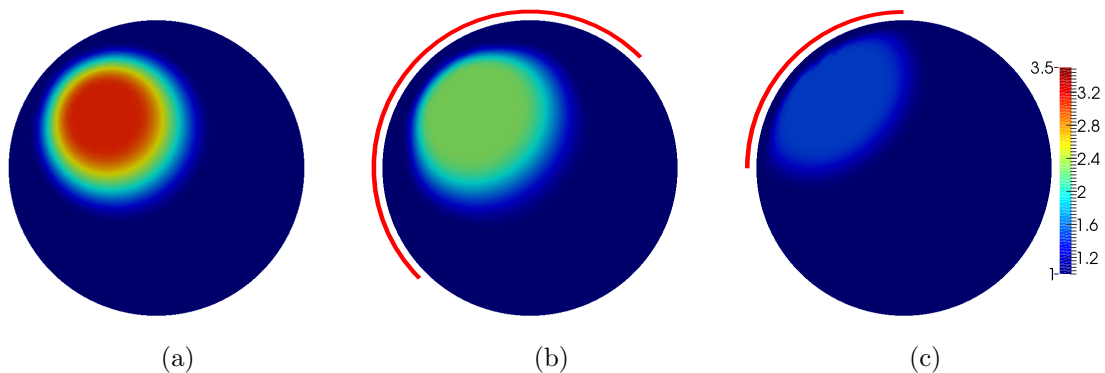


Figure 4.10. TV reconstruction of the phantom in figure 4.1(a). **(a)**: Full boundary data. **(b)**: 50% boundary data. **(c)**: 25% boundary data.

As seen from figure 4.10 and figure 4.11 the support of the inclusion is slightly overestimated in the case of full boundary data, and for the partial data cases the support is slightly larger than the counterparts in figure 4.8 and figure 4.9. It is also noticed that the TV reconstructions have a much lower contrast than the  $\ell_1$  sparsity reconstructions, and the contrast for the TV reconstructions is severely reduced when partial data is used. It is also observed that the same type of shape deformation occurs for both methods in case of partial data.

A typical feature of the TV regularization is piecewise constant reconstructions, however the reconstructions seen here have constant contrast levels with a smooth transition between them. There are several reason for this; and is due to the slight smoothing of the penalty term, but mostly because the discrepancy terms are not convex and may lead to local minima. The same kind of smooth transitions are also observed in TV-based methods for EIT in [45].

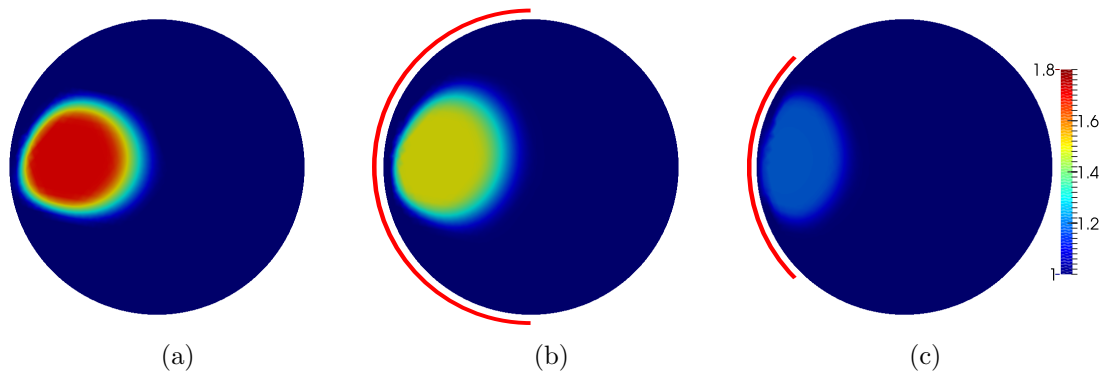


Figure 4.11. TV reconstruction of the phantom in figure 4.1(b). **(a)**: Full boundary data. **(b)**: 50% boundary data. **(c)**: 25% boundary data.

## 5. Conclusions

We have extended the algorithm developed in [33], for sparse reconstruction in electrical impedance tomography, to the case of partial data. Furthermore, we have shown how a distributed regularization parameter can be applied to utilize spatial prior information. This lead to numerical results showing improved reconstructions for the support of the inclusions and the contrast simultaneously. The use of the distributed regularization parameter enables sharper edges in the reconstruction and vastly reduces the deformation of the inclusions in the partial data problem, even when the prior is overestimated.

The algorithm can be generalized for 3D reconstruction, under further assumptions on the boundary conditions  $\{g_k\}_{k=1}^K$  and the amplitude of the perturbation  $\delta\sigma$ . This will be considered in a forthcoming paper [35].

## Funding

This research is supported by Advanced Grant No. 291405 HD-Tomo from the European Research Council.

## References

- [1] Holder DS. Electrical impedance tomography: Methods, history and applications. IOP Publishing Ltd, Bristol; 2005.
- [2] Abubakar A, Habashy TM, Li M, Liu J. Inversion algorithms for large-scale geophysical electromagnetic measurements. *Inverse Problems*. 2009;25(12):123012.
- [3] York TA. Status of electrical tomography in industrial applications. *Proceedings of the SPIE - the International Society for Optical Engineering*. 2001;4188:175–190.
- [4] Calderón AP. On an inverse boundary value problem. In: *Seminar on Numerical Analysis and its Applications to Continuum Physics (Rio de Janeiro, 1980)*. Rio de Janeiro: Soc. Brasil. Mat.; 1980. p. 65–73.
- [5] Sylvester J, Uhlmann G. A global uniqueness theorem for an inverse boundary value problem. *Ann of Math (2)*. 1987;125(1):153–169.
- [6] Nachman AI. Reconstructions from boundary measurements. *Ann of Math (2)*. 1988; 128(3):531–576.
- [7] Novikov RG. A multidimensional inverse spectral problem for the equation  $-\Delta\psi + (v(x) - Eu(x))\psi = 0$ . *Funktsional Anal i Prilozhen*. 1988;22(4):11–22, 96.
- [8] Nachman AI. Global uniqueness for a two-dimensional inverse boundary value problem. *Ann of Math (2)*. 1996;143(1):71–96.

- [9] Astala K, Päivärinta L. Calderón’s inverse conductivity problem in the plane. *Ann of Math* (2). 2006;163(1):265–299.
- [10] Haberman B, Tataru D. Uniqueness in Calderón’s problem with Lipschitz conductivities. *Duke Math J*. 2013;162(3):496–516.
- [11] Uhlmann G. Electrical impedance tomography and Calderón’s problem. *Inverse Problems*. 2009;25(12):123011.
- [12] Alessandrini G. Stable determination of conductivity by boundary measurements. *Appl Anal*. 1988;27(1-3):153–172.
- [13] Alessandrini G. Singular solutions of elliptic equations and the determination of conductivity by boundary measurements. *J Differential Equations*. 1990;84(2):252–272.
- [14] Mandache N. Exponential instability in an inverse problem for the Schrödinger equation. *Inverse Problems*. 2001;17(5):1435–1444.
- [15] Siltanen S, Mueller J, Isaacson D. An implementation of the reconstruction algorithm of A. Nachman for the 2D inverse conductivity problem. *Inverse Problems*. 2000;16(3):681–699.
- [16] Knudsen K, Lassas M, Mueller JL, Siltanen S. Regularized D-bar method for the inverse conductivity problem. *Inverse Probl Imaging*. 2009;3(4):599–624.
- [17] Bikowski J, Knudsen K, Mueller JL. Direct numerical reconstruction of conductivities in three dimensions using scattering transforms. *Inverse Problems*. 2011;27(1):015002, 19.
- [18] Delbary F, Hansen PC, Knudsen K. Electrical impedance tomography: 3D reconstructions using scattering transforms. *Appl Anal*. 2012;91(4):737–755.
- [19] Delbary F, Knudsen K. Numerical nonlinear complex geometrical optics algorithm for the 3D Calderón problem. *Inverse Probl Imaging*. 2014;8(4):991–1012.
- [20] Bukhgeim AL, Uhlmann G. Recovering a potential from partial Cauchy data. *Comm Partial Differential Equations*. 2002;27(3-4):653–668.
- [21] Kenig CE, Sjöstrand J, Uhlmann G. The Calderón problem with partial data. *Ann of Math* (2). 2007;165(2):567–591.
- [22] Knudsen K. The Calderón problem with partial data for less smooth conductivities. *Comm Partial Differential Equations*. 2006;31(1-3):57–71.
- [23] Zhang G. Uniqueness in the Calderón problem with partial data for less smooth conductivities. *Inverse Problems*. 2012;28(10):105008, 18.
- [24] Isakov V. On uniqueness in the inverse conductivity problem with local data. *Inverse Probl Imaging*. 2007;1(1):95–105.
- [25] Imanuvilov OY, Uhlmann G, Yamamoto M. The Calderón problem with partial data in two dimensions. *J Amer Math Soc*. 2010;23(3):655–691.
- [26] Heck H, Wang JN. Stability estimates for the inverse boundary value problem by partial Cauchy data. *Inverse Problems*. 2006;22(5):1787–1796.
- [27] Hamilton SJ, Siltanen S. Nonlinear inversion from partial EIT data: computational experiments. In: *Inverse problems and applications*. Vol. 615 of *Contemp. Math.*; Amer. Math. Soc., Providence, RI; 2014. p. 105–129.
- [28] Daubechies I, Defrise M, De Mol C. An iterative thresholding algorithm for linear inverse problems with a sparsity constraint. *Comm Pure Appl Math*. 2004;57(11):1413–1457.
- [29] Bredies K, Lorenz DA, Maass P. A generalized conditional gradient method and its connection to an iterative shrinkage method. *Comput Optim Appl*. 2009;42(2):173–193.
- [30] Bonesky T, Bredies K, Lorenz DA, Maass P. A generalized conditional gradient method for nonlinear operator equations with sparsity constraints. *Inverse Problems*. 2007;23(5):2041–2058.
- [31] Gehre M, Kluth T, Lipponen A, Jin B, Seppänen A, Kaipio JP, Maass P. Sparsity reconstruction in electrical impedance tomography: an experimental evaluation. *J Comput Appl Math*. 2012;236(8):2126–2136.
- [32] Jin B, Maass P. An analysis of electrical impedance tomography with applications to Tikhonov regularization. *ESAIM: Control, Optimisation and Calculus of Variations*. 2012 10;18:1027–1048.
- [33] Jin B, Khan T, Maass P. A reconstruction algorithm for electrical impedance tomography based on sparsity regularization. *Internat J Numer Methods Engrg*. 2012;89(3):337–353.
- [34] Borcea L. Electrical impedance tomography. *Inverse Problems*. 2002;18(6):R99–136.
- [35] Garde H, Knudsen K. 3D reconstruction for partial data electrical impedance tomography

- using a sparsity prior. Submitted. 2014; Available from: <http://arxiv.org/abs/1412.6288>.
- [36] Adams RA, Fournier JJF. Sobolev spaces. 2nd ed; Vol. 140 of Pure and Applied Mathematics (Amsterdam). Elsevier/Academic Press, Amsterdam; 2003.
  - [37] Neuberger JW. Sobolev gradients and differential equations. 2nd ed; Vol. 1670 of Lecture Notes in Mathematics. Berlin: Springer-Verlag; 2010.
  - [38] Barzilai J, Borwein JM. Two-point step size gradient methods. *IMA J Numer Anal.* 1988; 8(1):141–148.
  - [39] Wright SJ, Nowak RD, Figueiredo MAT. Sparse reconstruction by separable approximation. *IEEE Trans Signal Process.* 2009;57(7):2479–2493.
  - [40] Stampacchia G. Le problème de dirichlet pour les équations elliptiques du second ordre à coefficients discontinus. *Annales de l'institut Fourier.* 1965;15(1):189–258.
  - [41] Kirsch A, Grinberg N. The factorization method for inverse problems. Vol. 36 of Oxford Lecture Series in Mathematics and its Applications. Oxford University Press, Oxford; 2008.
  - [42] von Harrach B, Ullrich M. Monotonicity-based shape reconstruction in electrical impedance tomography. *SIAM J Math Anal.* 2013;45(6):3382–3403.
  - [43] von Harrach B, Seo JK. Exact shape-reconstruction by one-step linearization in electrical impedance tomography. *SIAM J Math Anal.* 2010;42(4):1505–1518.
  - [44] Logg A, Mardal KA, Wells GN. Automated solution of differential equations by the finite element method. Vol. 84 of Lecture Notes in Computational Science and Engineering. Springer, Heidelberg; 2012; the FEniCS book.
  - [45] Borsic A, Graham BM, Adler A, Lionheart W. In vivo impedance imaging with total variation regularization. *IEEE Transactions on Medical Imaging.* 2010;29(1):44–54.